A novel method for interpreting potential field anomalies using the Rootsig function

Ahmad Alvandi [a] , Vahid E. Ardestani [a] , Seyed-Hani Motavalli-Anbaran [a, *]

[a] *Institute of Geophysics, University of Tehran, Iran.*

ABSTRACT

Potential field data play a crucial role in the interpretation of various geological structural features. The application of edge detection techniques significantly improves the capacity to delineate subsurface structures. In recent years, a variety of methodologies have been developed to identify edges; however, each of these methodologies possesses distinct advantages and limitations. This study presents a novel edge enhancement technique that employs the Total Horizontal Derivative (THD) in conjunction with the Rootsig activation function (RTHD). This technique is applied to the interpretation of potential field data to enhance structural mapping. The effectiveness of the RTHD is evaluated through the interpretation of synthetic gravity and magnetic anomalies, both with and without the presence of noise, including sources located at various depths. Furthermore, the RTHD technique is applied to investigate gravity field data from the Považský Inovec Mountains, located in the Western Carpathians of Slovakia. In this region, the boundaries of the primary anomalies, as well as the Považie and Ripňany faults, are distinctly delineated. The results demonstrate that the RTHD approach effectively delineates edges and balances the amplitudes of both shallow and deep-seated sources, in contrast to traditional edge enhancement methods. The findings indicate that the RTHD represents a more effective strategy for structural mapping when utilizing gravity and magnetic data.

Keywords: *Edge detection, Potential filed, Rootsig activation function, Slovakia territory.*

1. Introduction

Gravity and magnetic (potential field) methods are among the most widely utilized geophysical techniques for the examination of subsurface structures and tectonic features [1-8]. These potential field methods have diverse applications, including the exploration of mineral resources, hydrocarbon exploration, studies of crustal deformation, and the mapping of both surface and subsurface structures. A primary focus is placed on characterizing geological formations and comprehending various geological structural boundaries at varying depths. The identification of the edges of these subsurface sources and the delineation of their horizontal extents are of paramount importance [9-16]. Various methodologies are employed to ascertain the boundaries of potential field anomalies, with each filtering technique offering distinct advantages and limitations [17].

A widely used approach for detecting edges, known as the Total Horizontal Derivative (THD), was first introduced by [18]. The THD filter is less sensitive to noise and is more effective in identifying shallow geological sources. The peak amplitudes of the THD occur at the boundaries of geological contacts. The THD can be expressed as follows [18]:

$$\text{THD} = \sqrt{\left(\frac{\partial F}{\partial x}\right)^2 + \left(\frac{\partial F}{\partial y}\right)^2} \qquad (1)$$

where F represents the reduced-to-the-pole magnetic or gravity field, along with its first-order derivatives in the x and y directions, respectively [18-19].

The Analytical Signal Amplitude (ASA) is a commonly employed approach to delineate the edges of potential field anomalies. The ASA can be mathematically represented as follows [20-21]:

$$\text{ASA} = \sqrt{\left(\frac{\partial F}{\partial x}\right)^2 + \left(\frac{\partial F}{\partial y}\right)^2 + \left(\frac{\partial F}{\partial z}\right)^2} \qquad (2)$$

where $\frac{\partial F}{\partial z}$ is a first-order vertical gradient of F.

It is essential to emphasize that both the THD and AS methodologies have limitations in their ability to effectively equalize causative sources situated at varying depths [4, 16, 22-24]. To simultaneously identify the edges of both shallow and deep anomalies, a variety of phase-based or normalized filters have been introduced.

The tilt derivative (TDR) approach was originally introduced as a technique for identifying the boundaries of both deep and shallow anomalies [16, 23]. The amplitude of the TDR is positive over the source, exhibits zero amplitude at the edges, and is negative in all other areas. The variations in TDR amplitude are limited to a range of ±90 degrees (±1.5 radians). The TDR can be mathematically represented as follows [25]:

$$\text{TDR} = \tan^{-1}\left(\frac{\frac{\partial F}{\partial z}}{\sqrt{\left(\frac{\partial F}{\partial x}\right)^2 + \left(\frac{\partial F}{\partial y}\right)^2}}\right) \qquad (3)$$

[26] developed another phase-based filtering technique known as the theta map approach. This detector demonstrates minimal amplitude at the edges of the buried source. The variations in the theta map amplitude are characterized by a defined range, extending from 0 to 90 degrees. The theta can be mathematically represented as follows [26]:

$$\text{Theta} = \cos^{-1}\left(\frac{\sqrt{\left(\frac{\partial F}{\partial x}\right)^2 + \left(\frac{\partial F}{\partial y}\right)^2}}{\sqrt{\left(\frac{\partial F}{\partial x}\right)^2 + \left(\frac{\partial F}{\partial y}\right)^2 + \left(\frac{\partial F}{\partial z}\right)^2}}\right) \quad (4)$$

[27] introduced a modified relation of THD (MTHD) that employs high-order gradients of potential field data to improve the resolution of edge detection maps. The MTHD can be expressed as follows [27]:

$$\text{MTHD} = \sqrt{\left(\frac{\partial^2 F}{\partial z\,\partial x}\right)^2 + \left(\frac{\partial^2 F}{\partial z\,\partial y}\right)^2} \quad (5)$$

In Eq. (5), $\frac{\partial^2 F}{\partial z\,\partial x}$ and $\frac{\partial^2 F}{\partial z\,\partial y}$ represent the vertical derivatives of the field in the x and y directions, respectively. The maximum amplitudes of the MTHD are observed at the edges of geological structures.

[28] proposed a normalized approach for identifying edges, which is termed the tilt derivative of the total horizontal derivative (TDTH). The computation involved in this method can be expressed as follows [28]:

$$\text{TDTH} = \tan^{-1}\left(\frac{\left(\frac{\partial \text{THD}}{\partial z}\right)}{\sqrt{\left(\frac{\partial \text{THD}}{\partial x}\right)^2 + \left(\frac{\partial \text{THD}}{\partial y}\right)^2}}\right) \quad (6)$$

In relation (6), $\frac{\partial \text{THD}}{\partial x}$, $\frac{\partial \text{THD}}{\partial y}$ and $\frac{\partial \text{THD}}{\partial z}$ represent the derivatives of THD in the x, y, and z directions, respectively. The maximum amplitudes of the TDTH are detected over the boundaries of geological formations. The variations in TDTH amplitude are limited to a range of ±90 degrees (±1.5 radians).

The IMTHD represents the improved version of the MTHD (IMTHD), which further enhances edge detection through the application of amplitude maxima. The IMTHD approach is calculated as described by [29]:

$$\text{IMTHD} = \tan^{-1}\left(\frac{\sqrt{\left(\frac{\partial^2 F}{\partial z\,\partial x}\right)^2 + \left(\frac{\partial^2 F}{\partial z\,\partial y}\right)^2}}{\left|\frac{\partial^2 F}{\partial z^2}\right|}\right) \quad (7)$$

In Eq. (7), the Laplace relation is employed to calculate the second vertical gradient ($\frac{\partial^2 F}{\partial z^2}$), which helps mitigate noise:

$$\frac{\partial^2 F}{\partial z^2} = -\left(\frac{\partial^2 F}{\partial x^2} + \frac{\partial^2 F}{\partial y^2}\right) \quad (8)$$

[30] substituted the arctangent function in Eq. (6) with the arcsine function and utilized an alternative ratio of the horizontal and vertical derivatives of the analytic signal to formulate the MASA approach, which is defined as follows [30]:

$$\text{MASA} = \sin^{-1}\left(\frac{\frac{\partial \text{AS}}{\partial z}}{\sqrt{\left(\frac{\partial \text{AS}}{\partial x}\right)^2 + \left(\frac{\partial \text{AS}}{\partial y}\right)^2 + \left(\frac{\partial \text{AS}}{\partial z}\right)^2}}\right) \quad (9)$$

2. Proposed detector (RTHD)

This research introduces an edge detection approach that utilizes the Rootsig activation function [31-33] to improve the identification of edges related to magnetic and gravity causative sources. The Rootsig function displays a shape that closely resembles that of the arctangent function, as noted by [31]. The arctangent function is commonly used in the context of edge detection for potential field data [16, 24]. We have introduced a novel methodology designed to enhance the resolution and accuracy of delineated edges by improving the total horizontal derivative approach. The proposed methodology utilizes an improved combination of the ratio of the first-order vertical and horizontal gradients of the total horizontal derivative of both reduced-to-pole (RTP) magnetic and gravity data. This Rootsig detector (RTHD) is defined in Eq. 10:

$$\text{RTHD} = \frac{(M-1)}{1+(\sqrt{1+M^2})} \quad (10)$$

where

$$M = \left(\frac{4 \times \frac{\partial \text{THD}}{\partial z}}{\sqrt{\left(\frac{\partial \text{THD}}{\partial x}\right)^2 + \left(\frac{\partial \text{THD}}{\partial y}\right)^2}} - \frac{1}{2}\right) \quad (11)$$

The amplitude of the RTHD ranges from -1 to 1, with amplitude maxima situated at the edges of the causative sources. A notable advantage of the RTHD is its ability to delineate edges with remarkable precision and clarity. In contrast to the proposed high-resolution techniques, the resolution of the RTHD results remains unaffected by the parameters selected by the interpreter [10, 23, 34-36].

3. Mitigating the effect of noise

The horizontal derivatives of the potential field are computed utilizing the finite-difference (FD) method, as described by [37]. This paper employs the finite-difference (FD) method, as introduced by [38], to compute first- and second-order vertical derivatives, thereby mitigating the effect of noise [39].

In the Cartesian coordinate system, let us consider the function F(x, y, z) as representing a potential field measured at a height z, where the positive z-axis is oriented vertically downward. The upward continuation fields (Fx, y, z − ΔL), (Fx, y, z − 2nΔL),..., (Fx, y, z − ΔL) at the heights ΔL, 2ΔL, ... , mΔL, with n = m = 1,2,3... N, are described by [37]:

$$\begin{cases} F(-\Delta L) = F - \Delta L \frac{\partial F}{\partial z} + \frac{(-\Delta L)^2}{2!}\frac{\partial^2 F}{\partial z^2} + \cdots + \frac{(-\Delta L)^n}{n!}\frac{\partial^n F}{\partial z^n} \\ F(-2\Delta L) = F - 2\Delta L \frac{\partial F}{\partial z} + \frac{(-2\Delta L)^2}{2!}\frac{\partial^2 F}{\partial z^2} + \cdots + \frac{(-2\Delta L)^n}{n!}\frac{\partial^n F}{\partial z^n} \\ \cdots \\ M(-m\Delta L) = F - n\Delta L \frac{\partial F}{\partial z} + \frac{(-n\Delta L)^2}{2!}\frac{\partial^2 F}{\partial z^2} + \cdots + \frac{(-n\Delta L)^n}{n!}\frac{\partial^n F}{\partial z^n} \end{cases} \quad (12)$$

with n = 3, Eq. (11) becomes:

$$\begin{cases} F(-\Delta L) = F - \Delta L \frac{\partial F}{\partial z} + \frac{(-\Delta L)^2}{2!}\frac{\partial^2 F}{\partial z^2} + \frac{(-\Delta L)^3}{3!}\frac{\partial^3 F}{\partial z^3} \\ F(-2\Delta L) = F - 2\Delta L \frac{\partial F}{\partial z} + \frac{(-2\Delta L)^2}{2!}\frac{\partial^2 F}{\partial z^2} + \frac{(-2\Delta L)^3}{3!}\frac{\partial^3 F}{\partial z^3} \\ F(-3\Delta L) = F - 3\Delta L \frac{\partial F}{\partial z} + \frac{(-3\Delta L)^2}{2!}\frac{\partial^2 F}{\partial z^2} + \frac{(-3\Delta L)^3}{3!}\frac{\partial^3 F}{\partial z^3} \end{cases} \quad (13)$$

Solving the above equations, vertical derivatives $\frac{\partial F}{\partial z}$ and $\frac{\partial^2 F}{\partial z^2}$ are given by:

$$\begin{cases} \frac{\partial F}{\partial z} = \frac{11F(x,y,z) - 18F(x,y,z-\Delta L) + 9F(x,y,z-2\Delta L) - 2F(x,y,z-3\Delta L)}{6\Delta L} \\ \frac{\partial^2 F}{\partial z^2} = \frac{2F(x,y,z) - 5F(x,y,z-\Delta L) + 4F(x,y,z-2\Delta L) - F(x,y,z-3\Delta L)}{6\Delta L^2} \end{cases} \quad (14)$$

In general, the value of ΔL is typically selected to be between 0.1 and 2 times the grid spacing, contingent upon the quality of the data [38]. In instances where the data is characterized by high levels of noise, the value of h exceeds twice the grid spacing [38]. In this work, the value of ΔL is equal to 0.1 times of the grid spacing for noise-free data, while for noisy data, it is selected to be five times greater than the grid spacing [38].

4. Synthetic data for a 2D model

A synthetic magnetic vertical dyke model, characterized by varying properties as detailed in Table 1, has been developed and is positioned at a depth of 5 km. The reduced-to-pole (RTP) magnetic response of this synthetic model is illustrated in Fig. 1a. The responses obtained from various conventional edge detection filters are depicted in Figs. 1b through 1j. It is evident from these responses that when the magnetic data is subjected to different conventional filters (Figs. 1b to 1j), the response is most effectively analyzed using the RTHD method (Fig. 1j). The maxima of the response are observed at the edges of the vertical dyke model. Additionally, a balanced image can be derived from the buried source.

Table 1. The parameters of the synthetic two-dimensional dyke-like model.

Parameters	Dyke-like
Number of stations	500
Depth of the dyke (in km)	5
Width (in km)	5
Strength of the Geomagnetic Field (nT)	35000
Inclination (°)	90
Declination (°)	0
Magnetic susceptibility (SI)	0.027
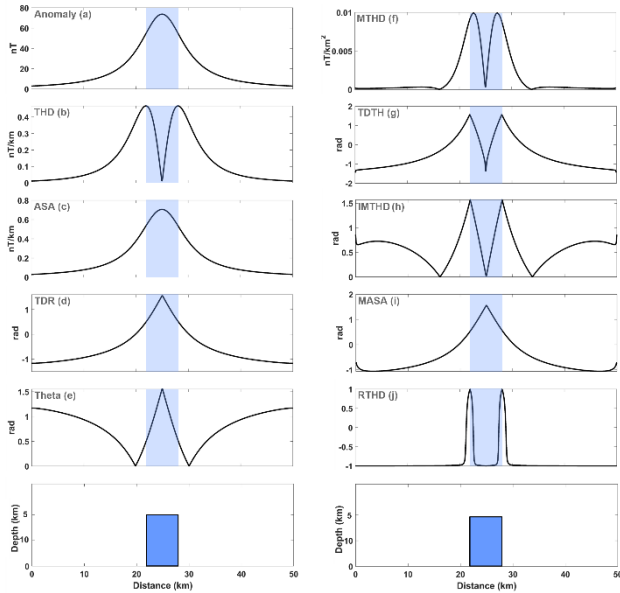
Fig. 1. A profile derived from a two-dimensional synthetic vertical dyke model, illustrating the following components: a) Magnetic anomaly, b) THD, c) ASA, d) TDR, e) Theta, f) MTHD, g) TDTH, h) IMTHD, i) MASA, and j) RTHD.

5. Synthetic data for 3D models
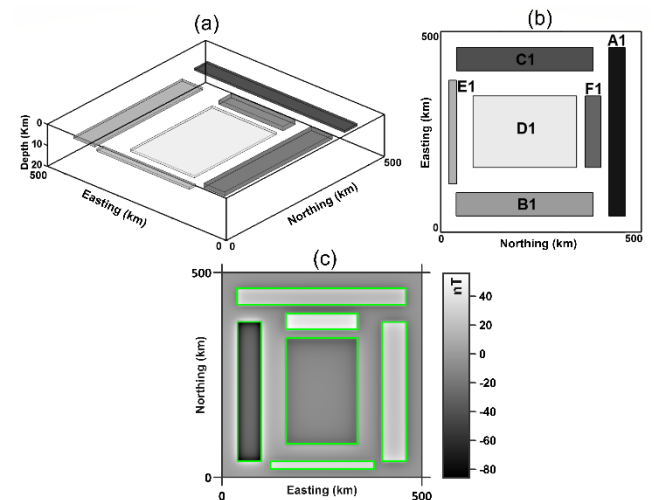
5.1. Magnetic model

To demonstrate the robustness of the proposed approach, a synthetic magnetic model consisting of six prismatic bodies has been constructed. The schematic representation of this synthetic magnetic model is depicted in Fig. 2a, and the nomenclature of the prismatic bodies is elaborated in Fig. 2b. The dimensions and characteristics of the prismatic bodies are presented in Table 2. The total magnetic intensity (TMI) is computed on a grid measuring 500×500 km², with a grid spacing of 1 km in both the east-west and north-south directions (Fig. 2c). The magnetic inclination and declination for all prisms are established at 90° and 0°, respectively. The magnetic anomaly is reduced to the pole, considering the specified inclination and declination (Fig. 2c). In all images, the green lines indicate actual edges.

The responses of the THD and ASA approaches are depicted in Figs. 3a and 3b, respectively. The response is primarily affected by shallow-seated bodies, whereas the boundaries related to deep-seated structures appear indistinct. The TDR approach, as shown in Fig. 3c, and the Theta technique depicted in Figure 3d have been observed to produce artifacts and false boundaries. The MTHD filter, represented in Fig. 3e, exhibits performance similar to that of the THD technique, failing to delineate the boundaries of deep sources effectively. In contrast, the TDTH method successfully delineates the boundaries of buried structures; however, a significant disadvantage of this method is its low-resolution edge map representation (Fig. 3f). The IMTHD (Fig. 3g) and MASA (Fig.

3h) maps also display false edges, and the resolution of the output images is inadequate, with spurious edges between the true edges, making interpretation complex. Conversely, the response of the RTHD filter, depicted in Fig. 3i, indicates that the proposed filter effectively delineates the edges of prismatic bodies situated at various depths, producing a well-balanced representation of these edges.

Table 2. The parameters of the synthetic dyke-like magnetic model.

Source/Label	A1	B1	C1	D1	E1	F1
y-coordinates of the center (in kilometres)	250	70	430	250	250	210
x-coordinates of the center (in kilometres)	440	210	210	210	30	380
Width (in kilometres)	40	60	60	180	20	40
Length (in kilometres)	420	340	340	260	260	260
Depth of the top (in kilometres)	4	3	6	7	5	6
Depth of the bottom (in kilometres)	5	5	7	8	6	8
Magnetization (A/m)	1	-1	1.6	-1.3	1.1	1

Fig. 2. a) A three-dimensional view of the first synthetic magnetic model, b) A planar view of the first synthetic magnetic model, and c) A magnetic anomaly map corresponding to the synthetic model (in nT).
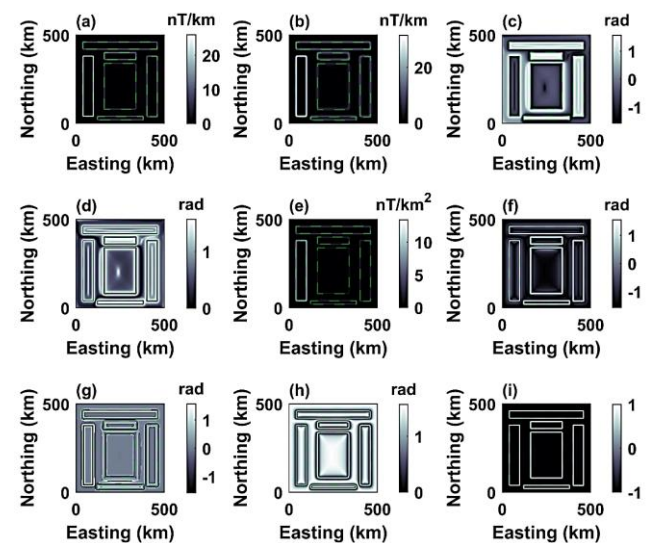
Fig. 3. The comparison of results obtained using various approaches alongside the proposed technique (Noise-free data): a) THD, b) ASA, c) TDR, d) Theta, e) MTHD, f) TDTH, g) IMTHD, h) MASA, and i) RTHD.

The stability of the proposed filter was evaluated by applying Gaussian noise to the magnetic anomaly, with a mean of zero and a standard deviation equivalent to 3% of the data's amplitude. It is important to note that any edge detection filter applied to the noisy data may not provide a clear representation of the subsurface structures [21]. Consequently, we employed the finite difference method [37] to mitigate noise, followed by the interpretation of the synthetic data using various filtering techniques. Fig. 4a-i illustrates the results of THD, ASA, TDR, Theta, MTHD, TDTH, IMTHD, MASA, and RTHD following the application of the finite difference (FD) technique. In a manner similar to the preceding scenario, conventional filters often render edges as blurred or generate false edges in the edge detection maps. In contrast, the proposed filter exhibits satisfactory performance in delineating the edges of buried structures.
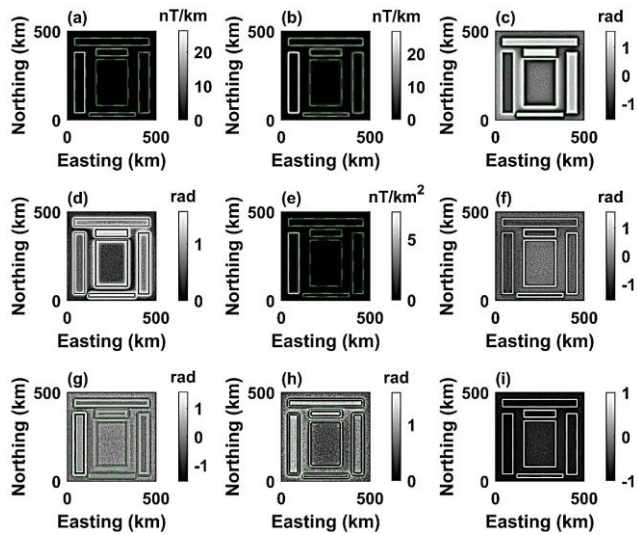
Fig. 4. The comparison of results obtained using various approaches alongside the proposed technique (noise-contaminated data). The approaches include: a) THD, b) ASA, c) TDR, d) Theta, e) MTHD, f) TDTH, g) IMTHD, h) MASA, and i) RTHD.
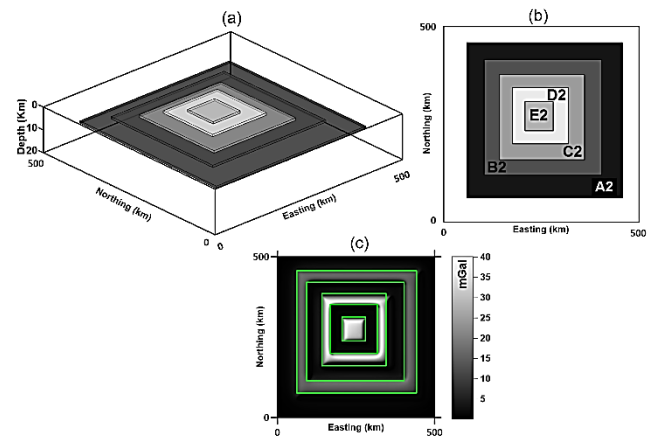
5.2. Gravity model

The synthetic gravity model is constructed using five prisms, each with distinct properties and buried at varying depths. A three-dimensional representation is provided in Fig. 5a, while the nomenclature for the five prisms utilized in the model is illustrated in Fig. 5b. The prisms (A2, B2, C2, D2, and E2) vary in size and depth; notably, two of the prisms (C2 and D2) have the same density. Prism A2 is located at a greater depth, whereas prism E2 is situated at a shallower depth. The model incorporates both positive and negative density contrasting bodies. The spatial and physical parameters of the second synthetic model are detailed in Table 3. The gravity field is calculated on a 500×500 km² grid, with a grid spacing of 1 km in both the east-west and north-south directions. The gravity anomaly generated over the synthetic model is depicted in Fig. 5c.

The responses of THD (Fig. 6a) and ASA (Fig. 6b) in relation to the gravity anomaly demonstrate that as the depth of burial of the prismatic bodies decreases, the filters produce sharper delineations. Nevertheless, both filters were ineffective in detecting the edges associated with deeper bodies. Figs. 6c and 6d illustrate the edge-drawing techniques utilizing the TDR and Theta methods. While both methods are applicable in this case, the resulting output resolution is inadequate, and spurious edges between the true edges make the interpretation complex. The results of edge detection employing the MTHD method are illustrated in Fig. 6e. Although this method serves as an improved filter compared to the THD, the edges of sources A2, B2, C2, and D2 remain undetected. Fig. 6f illustrates the delineation of boundaries for all sources, achieved through the application of the TDTH technique. It is noteworthy that the image resolution obtained via this method is

relatively low. Fig. 6g illustrates the results of edge determination using the IMTHD method. This approach demonstrates suboptimal performance in precisely delineating the boundaries of deep structures. In contrast, Fig. 6h employs the MASA method for edge determination. Although this technique effectively delineates the edges of the buried sources, it also reveals the presence of spurious boundaries between these sources. The response of the proposed approach is shown in Fig. 6i, and it provides high-resolution edges of the prismatic sources with no spurious edges between true edges. Clearly, this filter is more effective in producing a clear image of the edges than the other filters.

Table 3. The parameters of the second synthetic model.

Source/Label	A2	B2	C2	D2	E2
y-coordinates of the center (in kilometers)	260	265	267	270	270
x-coordinates of the center (in kilometers)	260	250	250	247	245
Width (in kilometers)	400	295	215	140	70
Length (in kilometers)	400	300	220	145	80
Depth of the top (in kilometers)	7	5	4	2	1
Depth of the bottom (in kilometers)	8	6	5	3	2
Density (g/cm³)	0.5	-0.5	1	1	-1

Fig. 5: a) A three-dimensional representation of the second synthetic gravity model, b) A planar representation of the second synthetic gravity model, and c) A gravity anomaly map corresponding to the synthetic model (in mGal).
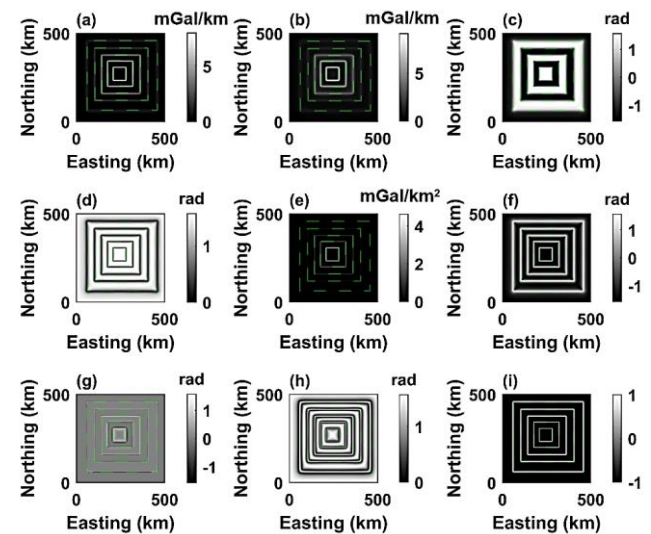
Fig. 6: The comparison of results obtained using various approaches alongside the proposed technique (Noise-free data): a) THD, b) ASA, c) TDR, d) Theta, e) MTHD, f) TDTH, g) IMTHD, h) MASA, and i) RTHD.

To further evaluate the stability of the proposed method, we implemented a corrupted gravity model that incorporated Gaussian noise with a mean of zero and a standard deviation equivalent to 3% of the data's amplitude, alongside the finite difference method, which mitigates the effect of noise on filter responses. Consistent with the observations derived from the noisy magnetic data, the RTHD filter (Fig. 7i) appears to effectively identify all edges with minimal noise interference, in contrast to the performance of other conventional filters (Fig. 7a-h).
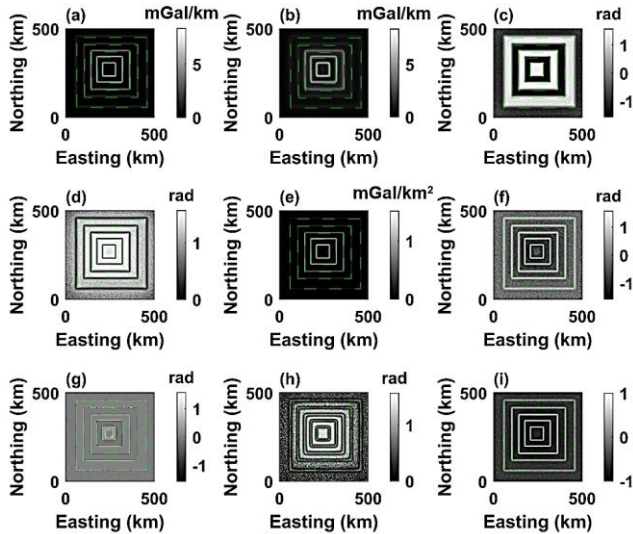
Fig. 7. The comparison of results obtained using various approaches alongside the proposed technique (noise-contaminated data). The approaches include: a) THD, b) ASA, c) TDR, d) Theta, e) MTHD, f) TDTH, g) IMTHD, h) MASA, and i) RTHD.

6. Application of RTHD to Real-World Data

In this section, the effectiveness of the RTHD approach is assessed utilizing real-world gravity data collected from the Považský Inovec Mountains, situated in the Western Carpathians. The Považský Inovec Mountains represent one of the horsts located within the northwestern segment of the internal Western Carpathians [40]. This mountain range is characterized by a crystalline basement belonging to the Tatricum, which is accompanied by a Late Paleozoic to Mesozoic sedimentary cover. Additionally, the region is overlain by two thin-skinned Mesozoic nappes, namely the Fatricum and Hronicum [40-41]. The Považie Fault and the Ripňany Fault represent the two primary geological faults within the study area. A simplified geological map of the Považský Inovec Mountains, located in the Western Carpathians, is presented in Fig. 8.
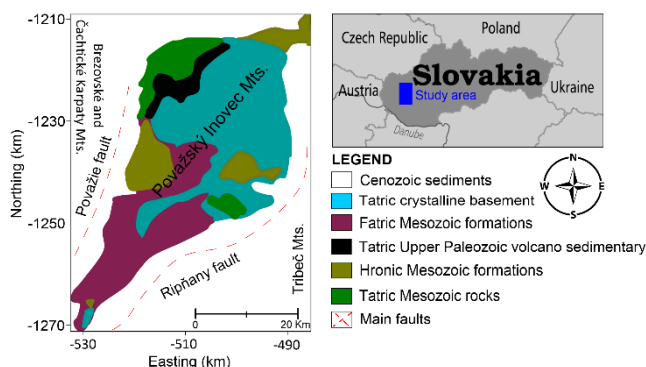
Fig. 8. The location of the study area and a simplified geological map of the Považský Inovec Mts. (based on [42-43]).

The complete Bouguer gravity data (SCBA) and the geological map are available online at no cost through the website of the State Geological Institute of Dionyza Stura in Bratislava (Fig. 9a). The gravimetric data obtained from the Slovak database exhibit acceptable quality and can be utilized with confidence for the interpretation of geological structures and in geodetic applications [36, 44]. To improve data quality and reduce noise, the FD method has been utilized prior to the implementation of edge detection filters (Fig. 10a-i).

The complete Bouguer gravity data (SCBA) and the geological map are available online at no cost through the website of the State Geological Institute of Dionyza Stura in Bratislava (Fig. 9a). The gravimetric data obtained from the Slovak database exhibit acceptable quality and can be utilized with confidence for the interpretation of geological structures and in geodetic applications [36, 44]. To improve data quality and reduce noise, the FD method has been utilized prior to the implementation of edge detection filters (Fig. 10a-i).
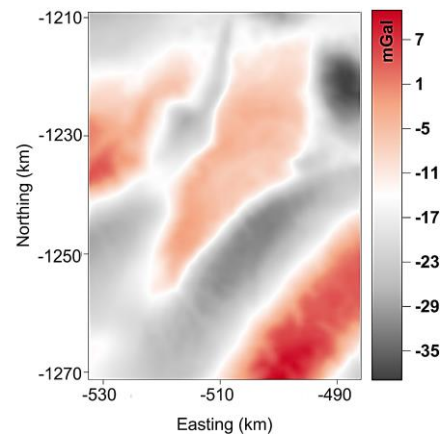

Fig. 9: Bouguer gravity data for the Považský Inovec Mts.

Figs. 10a and 10b present the results obtained from the THD and ASA approaches, respectively. As illustrated, the maps generated by both THD and ASA are blurred and unreliable in delineating clear edges for the subsurface sources. Figs. 10c and 10d illustrate the results obtained using the TDR and Theta techniques, respectively. As shown in these figs., both techniques effectively equalize the amplitudes of large and small anomalies. However, many adjacent boundaries produced by these methods are interconnected, which complicates the detection of geological structures. Fig. 10e illustrates the outcomes of edge detection utilizing the modified total horizontal gradient method. It is important to note that this filter is unable to simultaneously delineate various structures within the region that possess differing depths. Fig. 10f illustrates the results of edge detection using the TDTH technique. The boundaries of various structures are delineated by this filter. However, similar to the theoretical cases, the image resolution remains low. Figs. 10g and 10h illustrate the results obtained from the IMTHD and MASA filters. As expected, consistent with the synthetic cases, the outputs generated by these two filters do not improve the interpretability of the gravity data for the region under investigation. Fig. 10i illustrates the results obtained from applying the proposed method to the gravity map. This method is effective in detecting geological structures in the Považský Inovec Mountains region. Furthermore, it is important to note that the RTHD method produces results with higher resolution compared to other techniques.

To facilitate a more comprehensive interpretation of the region and delineate the characteristics of various subsurface structures at different depths, the 3D Euler deconvolution (ED) method has been employed [45-46]. The Euler deconvolution method is a widely used technique for interpreting potential field data [47]. To calculate the depth, a structural index of 0 and a window size equivalent to 17 times the grid cell size are used. The depths of these structures range from 1 km to 16 km. The depth map is illustrated in Fig. 11a, while the solution histogram of the depth map is presented in Fig. 11b.
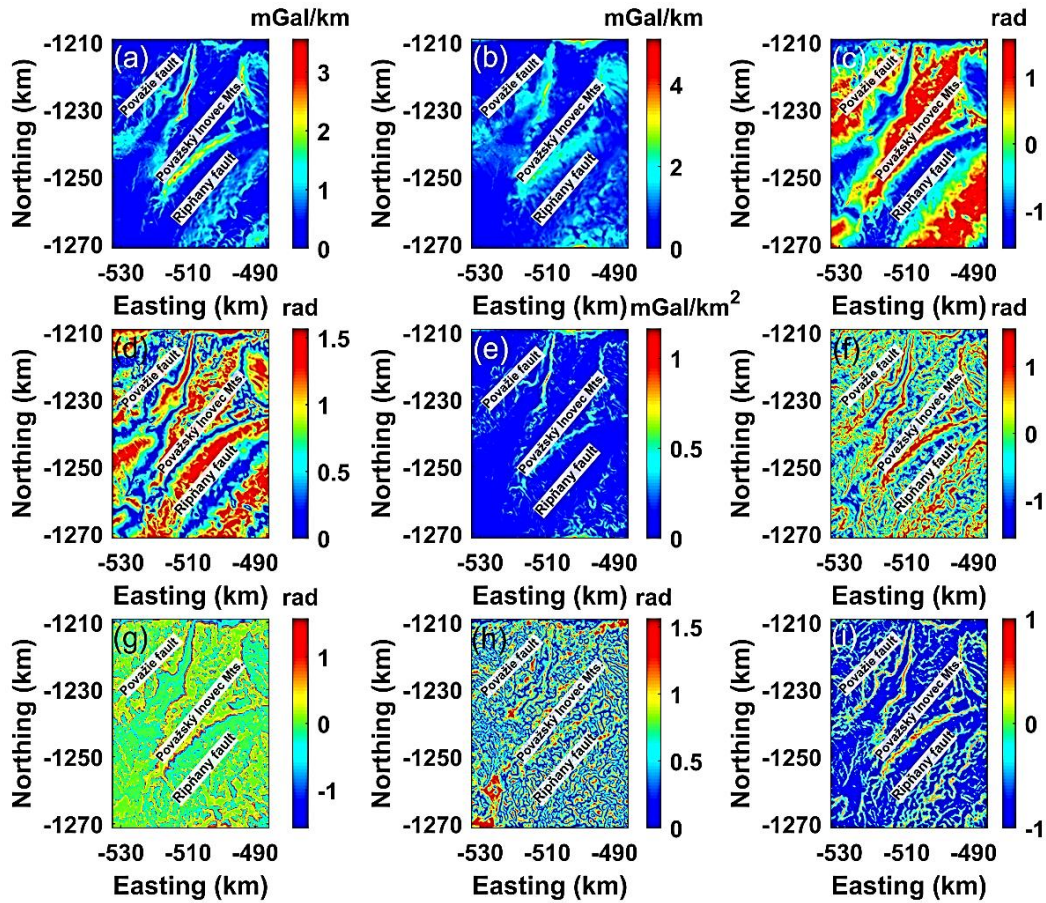
Fig. 10: A comparative analysis of the results obtained using various filters applied to the gravity data of the Považský Inovec Mountains following finite difference (FD) filtering: a) THD, b) ASA, c) TDR, d) Theta, e) MTHD, f) TDTH, g) IMTHD, h) MASA, and i) RTHD.
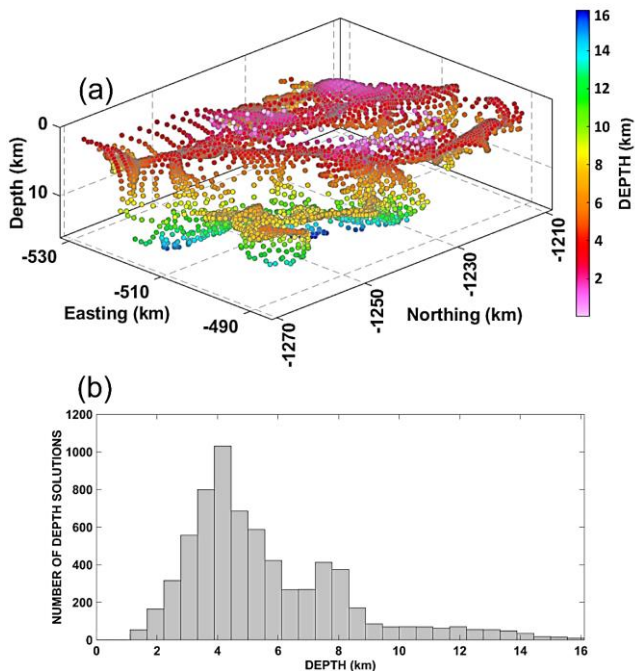
Fig. 11. a) Depths obtained through the 3D Euler deconvolution (ED) technique, and b) histogram of solutions representing the depths estimated using the Euler deconvolution method.

7. Conclusions

Edge enhancement is a fundamental process in the analysis and interpretation of subsurface structures. The accuracy of this process improves with the reduction of noise, which has led to an increased reliance on advanced filtering techniques. While edge enhancement filters are based on data derivatives and often amplify noise signals, the RTHD filter can simultaneously equalize both weak and strong signals without introducing false information into the edge map. In order to evaluate the performance of the proposed filter in comparison to conventional filters, we employed synthetic models both with and without noise. The results clearly demonstrate the effectiveness of the introduced filter in identifying the edges of buried sources. Furthermore, the RTHD filter establishes a strong correlation between the detected edge image and the geological map of the study area, thereby facilitating the construction of a structural framework. Ultimately, the RTHD filter provides higher resolution, eliminates false edges, and generates more nuanced geological features. In general, the proposed filter can be utilized in conjunction with the finite difference (FD) method to reduce noise in the interpretation of gravity and magnetic data, as well as to identify the edges of anomalies.

Acknowledgments

References

[1] Ghiasi, S. M., Hosseini, S. H., Afshar, A., & Abedi, M. (2023). A novel magnetic interpretational perspective on the Charmaleh iron deposit through improved edge detection techniques and 3D inversion approaches. Natural Resources Research, 32(1), 147-170.

[2] Fedi, M. (2007). DEXP: A fast method to determine the depth and the structural index of potential fields sources. Geophysics 72: I1–I11. https://doi.org/10.1190/1.2399452.

[3] Cella, F., Fedi, M., & G. Florio. (2009). Toward a full multiscale approach to interpret potential fields. Geophysical Prospecting 57: 543–57. https://doi.org/10.1111/j.1365-2478.2009.00808.x.

[4] Pham, L.T., Oksum, E., Do, T. D., & Le-Huy, M., (2018). New method for edges detection of magnetic sources using logistic function. Geofizicheskiy Zhurnal, 40(6), 127-135.

[5] Alvandi, A., Deniz Toktay, H., & Nasri, S. (2022). Application of direct source parameter imaging (direct local wave number) technique to the 2D gravity anomalies for depth determination of some geological structures. Acta Geophysica, 70, 659–667. https://doi.org/10.1007/s11600-022-00750-6.

[6] Al-Bahadily HA, Al-Rahim AM, & Smith RS. (2023). Determination of reactivated regions and faults in the Iraq Southern Desert with the new edge technique, Inverse Tilt Angle of Second-gradients (ITAS). Acta Geophysica 72:1675–1692.

[7] Ekinci YL, Balkaya Ç, Göktürkler G, & Ai H. (2023). 3-D gravity inversion for the basement relief reconstruction through modified success-history-based adaptive differential evolution. Geophysical Journal International 235 (1): 377-400, https://doi.org/10.1093/gji/ggad222.

[8] Su, K, Ai, H, Alvandi, A, Lyu, C, Wei, X, Qin, Z, Tu, Y, Yan, Y & Nie, Tao. (2024). Hunger Games Search for the elucidation of gravity anomalies with application to geothermal energy investigations and volcanic activity studies, Open Geosciences, 16 (1). https://doi.org/10.1515/geo-2022-0641.

[9] Cooper, G.R.J. & Cowan, D.R. (2006). Enhancing potential field data using filters based on the local phase. Comput. Geosci.,32, 1585–1591.

[10] Cooper, G.R.J. (2009). Balancing images of potential field data. Geophysics, 74, L17–L20.

[11] Ekinci YL, & Yigitbas E. (2015). Interpretation of gravity anomalies to delineate some structural features of Biga and Gelibolu peninsulas, and their surroundings (north-west Turkey). Geodinam Acta 27(4):300–319

[12] Eldosouky AM, El-Qassas RAY, Pour AB, Mohamed H, & Sekandari M. (2021). Integration of ASTER satellite imagery and 3D inversion of aeromagnetic data for deep mineral exploration. Adv Space Res 68(9):3641–3662.

[13] Eldosouky AM, Pham LT, & Henaish A. (2022). High precision structural mapping using edge filters of potential field and remote sensing data: a case study from Wadi Umm Ghalqa area, South Eastern Desert, Egypt. The Egyptian Journal of Remote Sensing and Space Science 25 (2): 501-513.

[14] Pham LT. (2024). An improved edge detector for interpreting potential field data. Earth Science Informatics.

[15] Deniz Toktay, H., Prasad, K. N. D., & Alvandi, A. (2024). Edge enhancement of potential field data using the enhanced gradient (EG) filter. Bulletin of the Mineral Research and Exploration, 174(174), 55-66. https://doi.org/10.19111/bulletinofmre.1386653.

[16] Ai, H., Deniz Toktay, H., Alvandi, A., Pasteka, R., Su, K., & Liu, Q. (2024). Advancing potential field data analysis: the Modified Horizontal Gradient Amplitude method (MHGA). Contributions to Geophysics and Geodesy, 54(2), 119-143. https://doi.org/10.31577/congeo.2024.54.2.1.

[17] Pham LT. (2023). A novel approach for enhancing potential fields: application to aeromagnetic data of the Tuangiao, Vietnam. The European Physical Journal Plus 138: 1134. https://doi.org/10.1140/epjp/s13360-023-04760-1.

[18] Cordell L, Grauch VJS. (1985). Mapping basement magnetization zones from aeromagnetic data in the San Juan basin, New Mexico. In: Hinze WJ (ed) The utility of regional gravity and magnetic anomaly society of exploration geophysics, p 181–197.

[19] Blakely J. R., & Simpson W.R., (1986). Approximating edges of source bodies from magnetic or gravity anomalies. Geophysics, 51(7), 1494-1498.

[20] Nabighian, M.N., (1984). Toward a tree dimensional automatic interpretation of potential field data via generalized Hilbert transforms: Fundamental relations. Geophysics, 49(6), 780-786.

[21] Roest, W.R.J., Verhoef, J., & Pilkington, M., (1992). Magnetic interpretation using the 3-D analytic signal. Geophysics, 57(1), 116-125.

[22] Prasad, K.N.D., Pham, L.T., & Singh, A.P., (2022). Structural mapping of potential field sources using BHG filter. Geocarto International, 37, 1-22, https://doi.org/10.1080/10106049.2022.2048903.

[23] Alvandi A, Ardestani V.E. (2023) Edge detection of potential field anomalies using the Gompertz function as a high-resolution edge enhancement filter. Bulletin of Geophysics and Oceanography 64: 279–300.

[24] Alvandi A, Su K, Ai H, Ardestani VE, & Lyu C. (2023a). Enhancement of potential field source boundaries using the hyperbolic domain (Gudermannian Function). Minerals 13: 1312.

[25] Miller H. G., & Singh V. (1994). Potential field tilt A new concept for location of potential field sources. Journal of Applied Geophysics, 32, 213-217.

[26] Wijns, C. Perez, C. & Kowalczyk, P., (2005). Theta map: Edge detection in magnetic data. Geophysics, 70, L39-L43.

[27] Tatchum, N.C., Tabod, C. T., Koumetio, F., & Manguelle – Dicoum, E. (2011). A gravity model study for differentiating vertical and dipping geological contacts with application to a Bouguer gravity anomaly over the Foumban shear zone, Cameroon. Geophysica, 37, 33-55.

[28] Ferreira, F.J.F., de Souza, J., Bongiolo, A.B.S., & Castro, L.G. (2013). Enhancement of the total horizontal gradient of magnetic anomalies using the tilt angle. Geophysics, 78, 33–31. https://doi.org/10.1190/geo2011-0441.1.

[29] Ma, G., Huang, D., & Liu, C., (2016). Step-edge detection filters for the interpretation of potential field data. Pure Appl. Geophys. 173 (3), 795–803.

[30] Ibraheem, I.M.; Aladad, H.; Alnaser, M.F. and Stephenson, R.

(2021). IAS: A New Novel Phase-Based Filter for Detection of Unexploded Ordnances. Remote Sensing, 13, 4345.

[31] Duch W, & Jankowski N. (1999). Survey of neural transfer functions. Neural Comput Appl 2:163–212

[32] da S. Gomes, G.S., Ludermir, T.B. & Lima, L.M.M.R. (2011). Comparison of new activation functions in neural network for forecasting financial time series. Neural Comput & Applic 20, 417–439.

[33] Farzad, A., Mashayekhi, H. & Hassanpour, H. (2019). A comparative performance analysis of different activation functions in LSTM networks for classification. Neural Comput & Applic 31, 2507–2521.

[34] Pham LT, Oksum E, Do TD, Le-Huy M, Vu MD, & Nguyen VD. (2019). LAS: a combination of the analytic signal amplitude and the generalized logistic function as a novel edge enhancement of magnetic data. Contrib Geophys Geod 49(4):425–440.

[35] Nasuti, Y., Nasuti, A., & Moghadas, D. (2019). STDR: A novel approach for enhancing and edge detection of potential field data. Pure and Applied Geophysics, 176, 827–831. https://doi.org/10.1007/s00024-018-2016-5.

[36] Alvandi, A., Deniz Toktay, H., & Ardestani, VE. (2023b). Edge detection of geological structures based on a logistic function: a case study for gravity data of the Western Carpathians. International Journal of Mining and Geo-Engineering, 57(3), 267-274. https://doi.org/10.22059/ijmge.2023.353516.595018.

[37] Ekinci YL, Ertekin C, & Yigitbas E. (2013). On the effectiveness of directional derivative based filters on gravity anomalies for source edge approximation: synthetic simulations and a case study from the Aegean graben system (western Anatolia, Turkey), Journal of Geophysics and Engineering 10:1742-2132.

[38] Tran KV, & Nguyen TN. (2020). A novel method for computing the vertical gradients of the potential field: application to downward continuation, Geophysical Journal International 220:1316–1329.

[39] Oliveira SP, & Pham LT. (2022). A stable finite difference method based on upward continuation to evaluate vertical derivatives of potential field data. Pure Appl Geophys 179(12):4555–4566.

[40] Hók, J., Šujan, M., & Šipka, F., (2014). Tectonic division of the Western Carpathians: an overview and a new approach. Acta Geol. Slovaca, 6(2), 135-143 (in Slovak, English summary).

[41] Pelech, O., Kušnirák, D., Bošanský, M., Dostál, I., Putiška, R., Hók, J., (2017). The resistivity image of the Upper Cretaceous Horné Belice Group: a case study from the Hranty section (Považský Inovec Mts., Western Carpathians). Acta Geologica Slovaca, 8, 43–58.

[42] Ivanička, J., Havrila, M., Kohút, M., Kováčik, M., Madarás, J., Olšavský, M., Hók, J., Polák, M., Filo, I., Elečko, M., Fordinál, K., Maglay, J., Pristaš, J., Buček, S. & Šimon, L., 2007: Geologická mapa Považského Inovca a jv. časti Trenčianskej kotliny 1: 50 000. Štátny geologický ústav Dionýza Štúra a Ministerstvo životného prostredia, Bratislava.

[43] Šujan, S., Rybár, M., Kováč, M., Bielik, D., Majcin, J., Minár, D., Plašienka, P., Nováková, J., Kotulová, 2021. The polyphase rifting and inversion of the Danube Basin revised Glob. Planet. Chang., 196.

[44] Zahorec P., Pašteka R., Mikuška J., Szalaiová V., Papčo J., Kušnirák D., Pánisová J., Krajňák M., Vajda P., Bielik M., Marušiak I., 2017: Chapter 7 – National Gravimetric Database of the Slovak Republic. In: Paˇsteka R., Mikuˇska J., Meurers B. (Eds.): Understanding the Bouguer Anomaly: A Gravimetry Puzzle. Elsevier, Amsterdam, 113–125, doi: 10.1016/B978-0-12-812913-5.00006-3.

[45] Florio, G., Fedi, M & Pasteka, R. (2006). On the application of Euler deconvolution to the analytic signal. Geophysics 71, no. 6: L87–L93. https://doi.org/10.1190/1.2360204.

[46] Cooper, G.R.J. & Whitehead, R.C. (2016). Determining the distance to magnetic sources. Geophysics, 81(2), J39–J48.

[47] Cooper, G.R.J. (2020). Iterative Euler deconvolution. Exploration Geophysics, 52(4), 468–474. https://doi.org/10.1080/08123985.2020.1834381.